ACS APPLIED MATERIALS & INTERFACES

www.acsami.org

Research Article

First-Principles Study of the Structural, Electronic, and Enhanced Optical Properties of SnS/TaS_2 Heterojunction

Arzoo Hassan, Muhammad Azhar Nazir, Yiheng Shen, Yaguang Guo,* Wei Kang, and Qian Wang*

Cite This: *ACS Appl. Mater. Interfaces* 2022, 14, 2177−2184

Read Online

ACCESS | Metrics & More | Article Recommendations | Supporting Information

ABSTRACT: Although the electronics and optoelectronics based on two-dimensional (2D) SnS have attracted great interest, their development is hindered by the large contact resistance at the interface of the metal−semiconductor junction. In this work, using first-principles calculations, we evaluate the contact performance in a van der Waals heterostructure composed of 2D SnS and TaS_2. We demonstrate that holes can freely transfer from the electrode to the channel as a consequence of the Schottky-barrier-free interface as well as an upward band bending. Moreover, we show that the intrinsic properties of the SnS monolayer are well-preserved in the heterojunction, which is different from those of contact with metal surfaces. An enhanced optical response is also observed as compared with the freestanding sheet. Given the recent experimental synthesis of the SnS−TaS_2 superlattice, this study enhances the understanding of the interface properties of SnS-based metal contact, which is essential for future device applications.

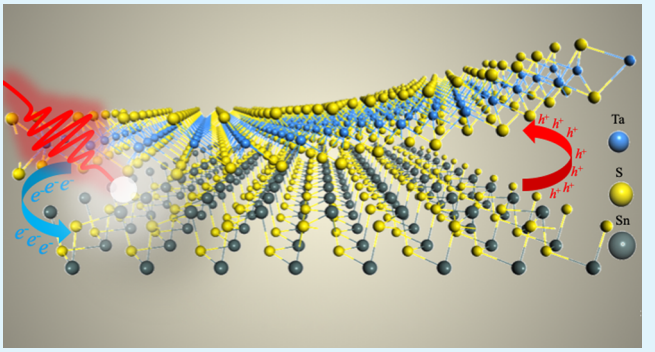

KEYWORDS: *heterostructure, TaS_2 monolayer, Ohmic contact, Schottky barrier, dielectric function, optical absorption*

INTRODUCTION

Bulk tin sulfide (SnS) belongs to the family of group IV monochalcogenides, which have been demonstrated to have huge potentials in thermoelectric[1−3] and earth-abundant thin-film solar cell applications.[4−7] Benefitting from the van der Waals (vdW) layered structure, the monolayer SnS has been synthesized through various experimental techniques, such as physical vapor transport,[8] thermodecomposition,[9] liquid exfoliation,[10] and facile solvothermal method.[11] Previous studies demonstrated that two-dimensional (2D) SnS and SnS_2 are promising candidates for electronics and optoelectronics because of their optical band gaps of 1.44 and 2.70 eV with high carrier mobility (~8.8×10^3 and 2.1×10^3 cm^2 V^{-1} s^{-1}), respectively, as well as strong light absorption characteristics reaching up to 10^5 cm^{-1} in the visible range (390−540 nm). More importantly, the inversion symmetry of the 2D black phosphorus (BP) configuration is broken by the two elements of SnS; therefore, richer physics, like giant piezoelectricity,[12] ferroelectricity,[12,13] second harmonic generation,[14] is discovered, which opens an avenue to design multifunctional devices.[15]

For practical applications, the interface of a metal contact plays a crucial role in determining the device's performance. While a lot of studies focus on the contacts in graphene and transition-metal dichalcogenide (TMDC),[16] less attention has been paid to the monolayer SnS experimental observations, suggesting that Cr and Ti can form ohmic contacts with the SnS nanoribbon,[17] but a first-principles study pointed out that the intrinsic semiconducting properties are destroyed when putting the SnS monolayer on the metal surfaces,[18] which could harm the carrier transport. For other metals, the strong Fermi level pinning (FLP)[18] becomes the major issue as in conventional metal−semiconductor junctions, leading to an untunable Schottky barrier between the electrode and the channel region, which in turn severely hinders the development of 2D SnS integrated devices. From this point of view, the vdW contact could provide an alternative solution because the weak interaction can reduce the FLP at the interface and keep the material properties intact at both sides,[19] hence making it easier to modulate the Schottky barrier height. Due to the highly tunable Fermi level, graphene is considered an ideal metal electrode. Indeed, many 2D materials, such as h-BN,[20,21] MoS_2,[22−24] and BP,[25,26] can exhibit novel carrier transport properties when stacked with graphene. Similarly, a theoretical work showed that the external electric field can induce the transition from Schottky contact to Ohmic contact in SnS-graphene-based heterojunction.[27] However, electrostatic doping in such a model is unlikely to be adopted for practical

Received: August 22, 2021
Accepted: December 9, 2021
Published: December 23, 2021

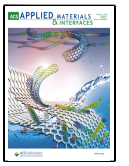

https://doi.org/10.1021/acsami.1c16020
ACS Appl. Mater. Interfaces 2022, 14, 2177−2184

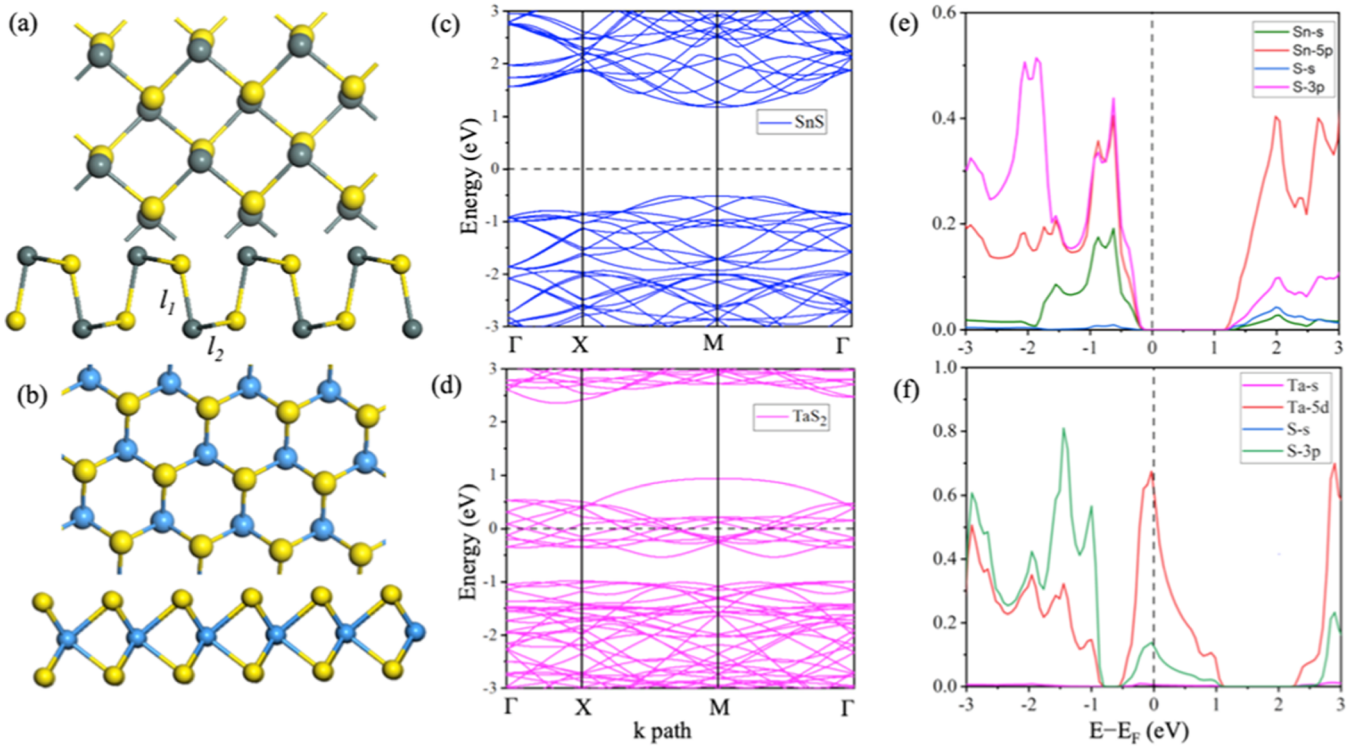

Figure 1. (a, b) Top and side views of the geometric structures, (c, d) band structures, and (e, f) partial DOS for the SnS and TaS_2 monolayers, respectively. The Fermi energy (E_f) is set to 0 eV. The yellow, gray, and blue spheres represent S, Sn, and Ta atoms, respectively.

application as it needs additional fabrication techniques at the source/drain regions. Therefore, a naturally formed Ohmic vdW SnS−metal heterojunction is preferred.

In this work, we demonstrate that the Schottky-barrier-free interface can be realized in a 2D SnS/TaS_2 heterostructure. Our idea comes from the recent experimental synthesis of a superlattice composed of SnS and TaS_2 with tunable architectures.[28] We note that TaS_2 is an emerging 2D layered transition-metal dichalcogenide (TMDC) with a structure similar to the 2H phase of MoS_2, but exhibiting different metallic properties,[29−31] and therefore could be used as an electrode. Based on density functional theory calculations, we systematically explore the geometric, electronic, and optical properties of the SnS/TaS_2 heterostructure. We strive to determine its interfacial properties, including charge transfer, Schottky barrier, band bending, and band alignment. Our calculations show that holes can be injected from TaS_2 to SnS efficiently at the heterojunction interface and enhanced optical properties of SnS can be achieved upon contact with TaS_2. Our findings indicate that the SnS/TaS_2 heterojunction is a promising candidate for future electronic and optoelectric applications.

COMPUTATIONAL METHODS

Our calculations are performed within the framework of density functional theory (DFT) using the projector-augmented-wave (PAW) potential as implemented in the Vienna *ab initio* Simulation Package (VASP).[32,33] The Perdew−Burke−Ernzerhof (PBE) electronic exchange-correlation functional[34] for the generalized gradient approximation (GGA) is used.[35] In addition, the van der Waals density functional of optB886-vdW is considered for all of the calculations to describe the effect of vdW interactions.[36,37] The valence electronic configurations for Sn, S, and Ta are taken as $5s^25p^2$, $3s^23p^4$, and $5d^36s^2$, respectively. A plane wave basis set with a cutoff energy of 500 eV is used for all of the calculations. The first Brillouin zone (BZ) is characterized with a fine-grid of $(3 \times 3 \times 1)$ for structural optimization and $(13 \times 13 \times 1)$ for static calculations, respectively.[38] A vacuum space of 25 Å along with the z-direction (perpendicular to SnS/TaS_2 heterojunction layers) is included to prevent the spurious interaction with duplicate images. The atomic positions are fully relaxed with an energy convergence criterion of 10^{-5} eV and force convergence of 0.01 eV/Å.[39] In addition, the thermal stability of the proposed structures is studied using ab initio molecular dynamics (AIMD) simulations, where the canonical ensemble (NVT) is employed and temperature control is achieved with the Nosé thermostat.[40] All optical properties can be deduced from the complex dielectric function $\varepsilon(\omega) = \varepsilon_1(\omega) + i\varepsilon_2(\omega)$. The imaginary part of complex dielectric function can be evaluated by momentum matrix relations between occupied and unoccupied wave functions, and $\varepsilon_1(\omega)$ can be calculated from $\varepsilon_2(\omega)$ using the Kramer−Kronig expressions[41]

$$\varepsilon_2(\omega) = \frac{2e^2\pi}{\Omega\epsilon_0} \sum_{k,v,c} |\langle \psi_k^c | \hat{u} \times \hat{r} | \psi_k^v \rangle|^2 \delta(E_k^c - E_k^v - E) \quad (1)$$

$$\varepsilon_1(\omega) = 1 + \left(\frac{2}{\pi}\right) \int_0^\infty \mathrm{d}\omega' \frac{\omega'^2 \varepsilon_2(\omega')}{\omega'^2 - \omega^2} \quad (2)$$

In the above equations, $\hat{u}$, e, ψ_k^c, and ψ_k^v are the vectors that describe the polarization of incident electric field, electronic charge, and the wave functions of the conduction band (CB) and the valance band (VB), respectively. Therefore, all other optical constants including absorption coefficient ($a(\omega)$), reflectivity ($R(\omega)$), energy loss function ($L(\omega)$), and the real part of optical conductivity ($\sigma(\omega)$) can be evaluated by the function of $\varepsilon(\omega)$ using the following formulas

$$a(\omega) = \sqrt{2}\omega[\sqrt{\varepsilon_1^2(\omega) + \varepsilon_2^2(\omega)} - \varepsilon_1(\omega)]^{1/2} \quad (3)$$

$$R(\omega) = \left| \frac{\sqrt{\varepsilon_1(\omega) + j\varepsilon_2(\omega)} - 1}{\sqrt{\varepsilon_1(\omega) + j\varepsilon_2(\omega)} + 1} \right|^2 \quad (4)$$

https://doi.org/10.1021/acsami.1c16020
ACS Appl. Mater. Interfaces 2022, 14, 2177−2184

$$L(\omega) = \mathrm{Im}\left(\frac{-1}{\varepsilon(\omega)}\right) = \frac{\varepsilon_2(\omega)}{\varepsilon_1^2(\omega) + \varepsilon_2^2(\omega)} \quad (5)$$

$$Re[\sigma(\omega)] = \frac{\omega}{4\pi}\varepsilon_2(\omega) \quad (6)$$

RESULTS AND DISCUSSION

Structure and Electronic Properties of SnS and TaS_2 Monolayers. Before focusing on the heterojunction properties, we first discuss the individual properties of the relaxed SnS and TaS_2 monolayers. As shown in Figure 1a, the SnS monolayer has an orthorhombic layered structure (*Pnma* group), with the lattice constants of the relaxed structure a = 4.03 Å and b = 4.23 Å and the bond length of l_1 = 2.54 Å and l_2 = 2.72 Å,[12,42] while the TaS_2 monolayer has a hexagonal 2H phase geometry, with the optimized lattice constants $a = b$ = 3.34 Å. All these results are in good agreement with the preceding studies.[43] Figure 1c–f plots the electronic structures of SnS and TaS_2. The band diagrams depict that SnS is a semiconductor with an indirect band gap of 1.60 eV, while TaS_2 exhibits metallic behavior as the partially occupied energy bands across the Fermi level. The partial density of states (DOS) of SnS shows that the valance band maximum (VBM) has a major contribution by *p* states of S atoms, whereas the p orbital of Sn atoms contributes to the conduction band minimum (CBM). While the *d* electrons act as the conducting electrons contributing to the metallic behavior of monolayer TaS_2. The s orbitals of S and Ta do not have a significant contribution to the states near the Fermi level both in SnS and TaS_2 monolayers.

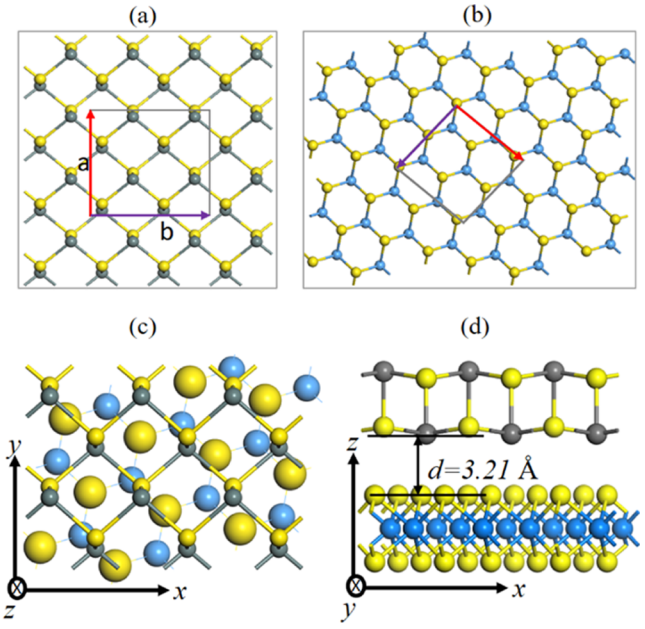

Figure 2. Top view of the supercells of (a) SnS and, (b) TaS_2. The lattice vectors are shown by red and purple lines. (c) Top view and (d) side view of the SnS/TaS_2 heterojunction.

Stability of the SnS/TaS_2 Heterojunction. Motivated by the preparation of the SnS/TaS_2 superlattice,[28] here we construct the SnS/TaS_2 heterojunction by vertically stacking the two monolayers together (see Figure 2). Due to the different lattice symmetries, the lattice match is carefully handled using our in-house code,[39] where the mismatch is set to be less than 3% to reduce the internal strain. For saving the computing cost, we have built several stacking structures with the minimum number of atoms. The selected configuration is illustrated in Figure 2, where 2 × 2 supercells of both SnS and TaS_2 are combined together with a lattice mismatch of 2.01%. To examine the interface stability of SnS/TaS_2, we have calculated its binding energy E_b defined by $E_b = (E_H - E_x - E_y)/A$, here E_H is the total energy of the SnS/TaS_2 heterojunction; E_x and E_y are the total energies of the individual SnS and the TaS_2 monolayer, respectively; and A is the area of the heterojunction. Figure 3a shows the binding energy E_b versus the interlayer distance, where the equilibrium distance is 3.21 Å with an E_b value of ∼38 meV/Å^2. The obtained E_b has the comparable magnitude as that of other vdW heterojunctions such as pentagraphene/graphene,[44] SnSe/graphene,[45] graphene/phosphorene,[19] and GeSe/SnSe heterojunctions.[46,47]

We then apply AIMD simulations using an NVT ensemble to study the thermal stability of the SnS/TaS_2 heterojunction. The fluctuation of the total energy at 500 K within each time step of 1 fs is plotted in Figure 3b. After 10 000 time steps, no obvious distortion in the geometry of the heterojunction is observed and the total potential energy remains almost constant during the entire simulation, confirming that the SnS/TaS_2 heterojunction is thermally stable.[48]

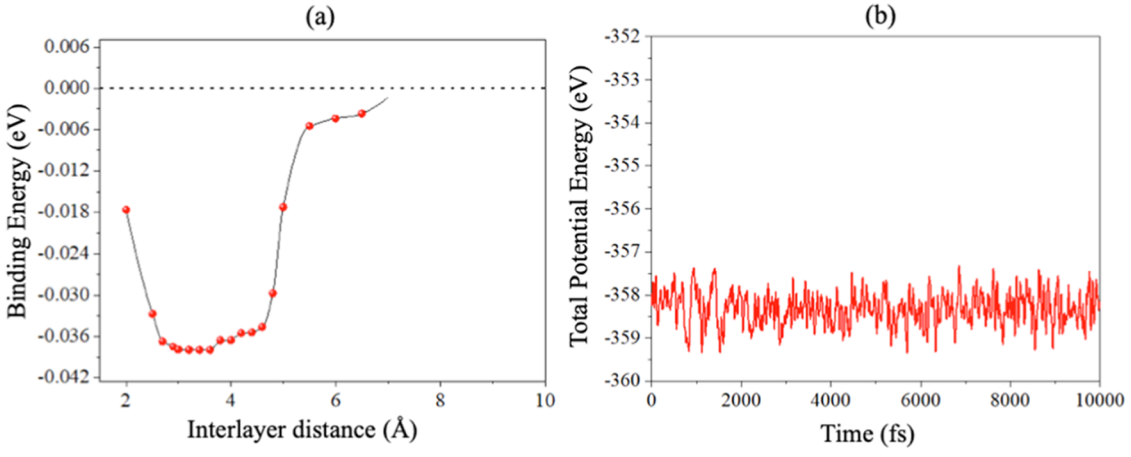

Figure 3. (a) Binding energy as a function of the interlayer distance, and (b) total potential energy fluctuation with the AIMD simulation time at 500 K for the SnS/TaS_2 heterostructure.

https://doi.org/10.1021/acsami.1c16020
ACS Appl. Mater. Interfaces 2022, 14, 2177−2184

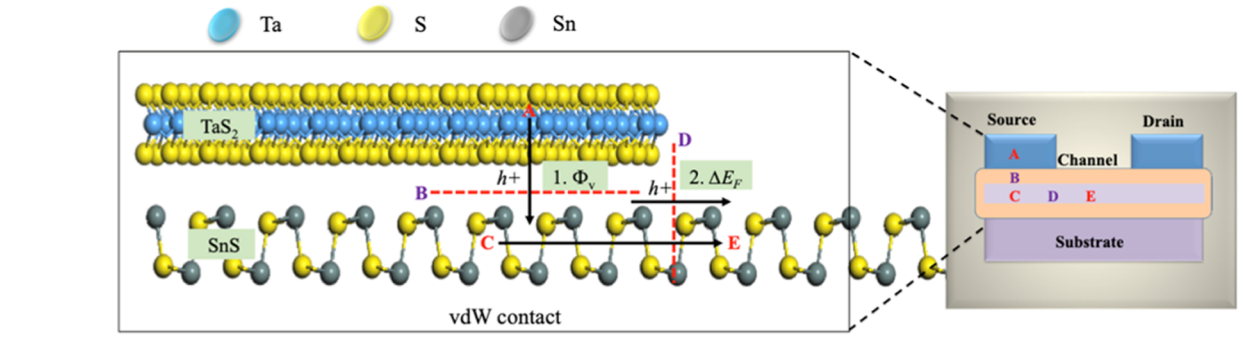

Figure 4. On the left side: a typical illustration of the SnS/TaS_2 heterojunction. A, C, and E represent the three regions, whereas B and D are the two distinguished interfaces. The black arrows show the pathway of an electron or holes moving from the metal electrode to the SnS channel (A to B to C to D to E). Φ_v is the Schottky barrier and ΔE_F is the band bending. The inset on the right side shows the schematic of a typical field effect transistor (FET), with source and drain contacts, and the channel region.

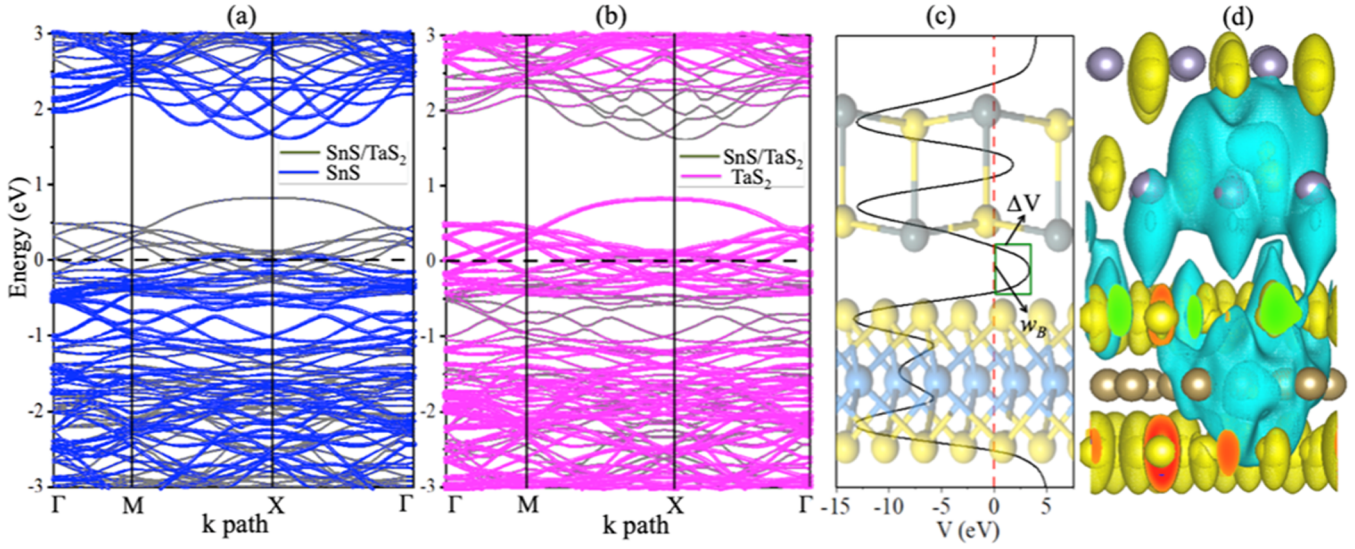

Figure 5. Projected band structures of (a) SnS and (b) TaS_2. The total band structure of the SnS/TaS_2 heterojunction is denoted by gray lines. The Fermi energy is shifted to zero. (c) Electrostatic potential profile along the *z*-direction, and (d) 3D isosurface electron density difference. The yellow and blue regions indicate the charge accumulation and depletion, respectively.

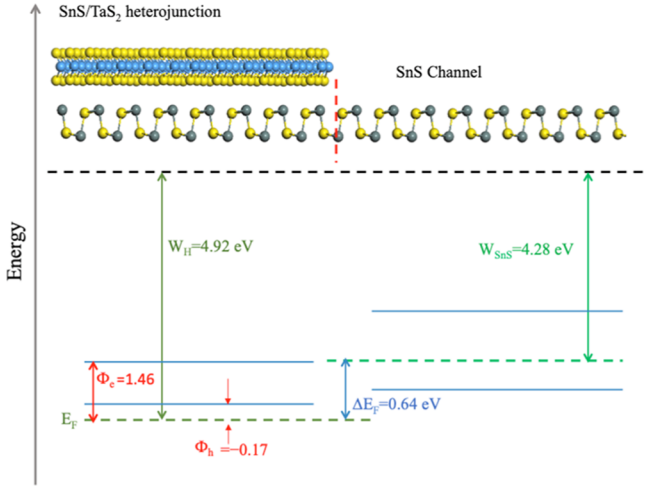

Figure 6. Band alignment in the SnS/TaS_2 heterojunction. The red dashed line represents the interface between the electrode and channel regions.

Interface Properties of the SnS/TaS_2 Heterojunction. From the device perspective, the carrier injection from metal to semiconductor is an important factor to determine the performance. As shown in Figure 4, the movement of charge carriers from the electrode to channel needs to overcome three types of barriers. Two of them are at the vertical interface B between the metal and the semiconductor in the heterojunction, called the Schottky barrier (Φ) and tunneling barrier, respectively. The other is at the lateral interface *D* between the heterojunction and the channel material (Φ_L), which can be evaluated by the band bending ΔE_F.[39] In the following, we will discuss them one by one.

The Schottky barrier is an essential parameter in determining the contact resistance. Following the Schottky−Mott rule,[45] the Schottky barrier height (SBH) is defined as the energy difference between the Fermi level (E_F) of the heterojunction and the respective energy band edges of the semiconductor, i.e., the CBM and the VBM identified from the projected band structure[19,49,50]

$$\Phi_{SB-n} = E_{CBM} - E_F, \quad \Phi_{SB-p} = E_F - E_{VBM} \tag{7}$$

where $\Phi_{SB\text{-}n}$ and $\Phi_{SB\text{-}p}$ are the n-type and p-type SBHs, respectively.[39] From Figure 5a, one can see that the Fermi level of the SnS/TaS_2 heterojunction goes into the valence bands of SnS with a $\Phi_{SB\text{-}p}$ value of −0.17 eV. This means that holes can

https://doi.org/10.1021/acsami.1c16020
ACS Appl. Mater. Interfaces 2022, 14, 2177−2184

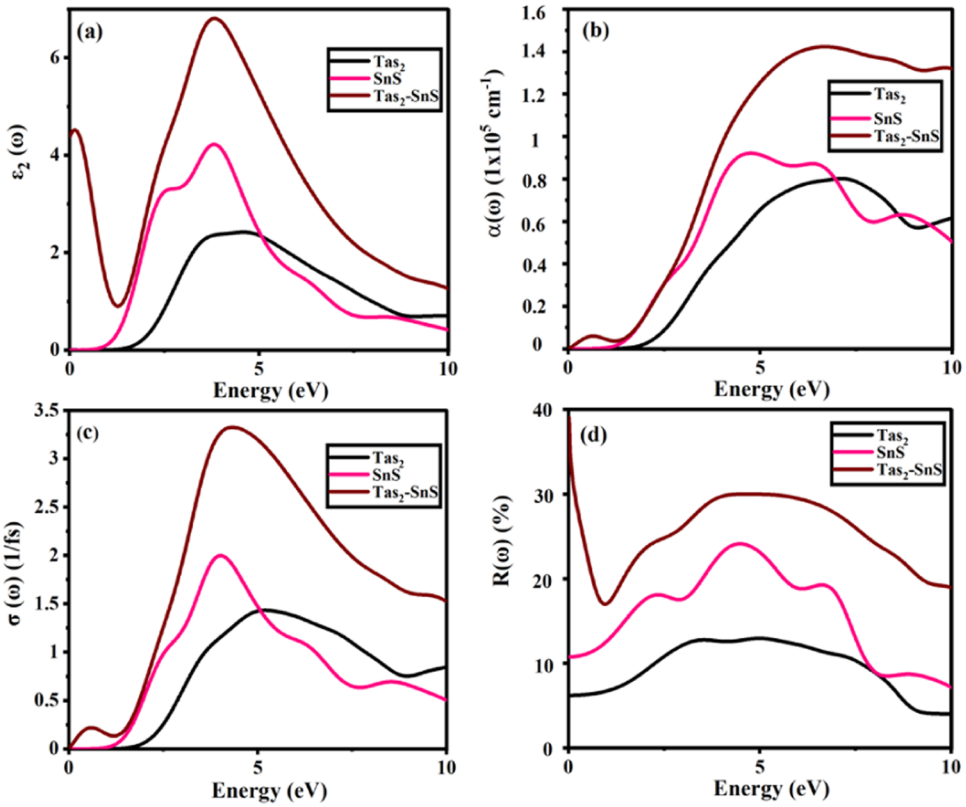

Figure 7. (a) Imaginary part of the dielectric function, (b) absorption coefficient, (c) optical conductivity, and (d) reflectivity percentage for SnS and TaS_2 monolayers and the SnS/TaS_2 heterojunction.

freely transfer from TaS_2 to SnS without any modulation, hence indicating an ohmic contact feature at the interface. In a recent experimental study, SnS_2 formed a Schottky contact with Au electrode with an SBH of ~38 meV for the charge carriers.[51] In comparison to that, a Schottky-barrier-free contact can show a better device performance. More importantly, it is worthy to note that the electronic properties of SnS are well-preserved upon contact (see Figure 1c,d for comparison). This further confirms that the SnS/TaS_2 heterojunction possesses the key of a vdW crystal, namely, keeping the intrinsic properties of the isolated parts intact. According to a previous study, the many-electron effects of the 2D channel semiconductor are strongly depressed. Thus, GGA functional is considered to be acceptable.[52]

In addition to the Schottky barrier, one can see from Figure 5c that there exists a tunneling barrier (TB) between the two surfaces upon forming the contact. Here, we use the WKB equation[46] to estimate the tunneling probability

$$T_B = \exp\left(-2\frac{\sqrt{2m\Delta V}}{\hbar} \times w_B\right) \quad (8)$$

where ΔV and w_B are the height and width of the tunneling barrier, respectively; m is the mass of the free electron; and $\hbar$ is the reduced Planck's constant. Here, we employ a square potential (marked by green lines) to approximately represent the barrier with an irregular shape. The predicted tunneling possibility is 26.67%, which is comparable to that of Rb_2PbX_4/graphene heterojunctions.[53] The relatively small value of tunneling possibility may result from the weak orbital overlap. In Figure 5d, we show the 3D isosurface of the electron density difference, where no obvious charge accumulation and depletion happen at the interface. This is consistent with the band structure that few new bands are formed as compared with the original one.

Next, we use the current-in-plane (CIP) model,[44] as shown in Figure 6, to estimate the band bending at interface D, which is determined by the energy difference in the Fermi level (ΔE_F) between that of the heterojunction and the freestanding sheet. Here, we set the vacuum level as the reference, and align other energy levels respective to it. According to the band alignment in Figure 6, one can see that the calculated work functions are 4.92 eV for heterojunction and 4.28 eV for the SnS monolayer; consequently, the band bending (ΔE_F) is predicted to be 0.64 eV. The positive ΔE_F suggests that the channel is p-type with holes as the major carriers. Together with the p-type Ohmic contact at interface B, it can be concluded that holes can be efficiently injected from TaS_2 to SnS.

Optical Properties. The interface interaction usually brings an enhanced optical response for the vdW heterostructure, which is beneficial for improving the performance of optoelectronic devices, such as solar cells and photodetectors. Here, we calculate the real and imaginary parts of the dielectric function, from which the absorption coefficient, optical conductivity, and reflectivity percentage are derived for monolayered SnS and TaS_2 and the SnS/TaS_2 heterojunction. For the SnS/TaS_2 system, as shown in Figure 6a, the imaginary part of the dielectric function is obviously improved and shows a larger value as compared to those of SnS and TaS_2 monolayers. As a result, the SnS/TaS_2 heterojunction exhibits a substantial absorption in both visible and near-UV regions (see Figure 7b). Specially, we find a peak of 0.5 eV, which is missing for the monolayer SnS, and its absorption coefficient can reach up to 10^5 cm^{-1} from ~3 eV. A similar phenomenon has also been

https://doi.org/10.1021/acsami.1c16020
ACS Appl. Mater. Interfaces 2022, 14, 2177−2184

observed in the phosphorene/TMDCs heterojunction.[42] The absorption peak at 0.5 eV can be attributed to the hybridized states near the Fermi level induced by the weak vdW interaction between SnS and TaS_2 through the overlap of the orbitals of the two consisting layers, hence providing the addition channels for dipole transition. In addition, we observe that the conductivity of the SnS/TaS_2 heterojunction starts at 0.5 eV because of the reduced intrinsic energy gap between the VB and CB (Figure 4). The conductivity of the SnS/TaS_2 heterojunction starts to increase from the visible region (1.5 eV), and the maxima of optical conductivity are identified from 4.3 eV in the near-ultraviolet region with the corresponding conductivity intensity $\sim 3.39\times10^5$ cm^{-1}, respectively. The reflectivity percentage of the SnS/TaS_2 heterojunction is increased twice compared with those of the freestanding SnS and TaS_2. The maximum reflection of the SnS/TaS_2 heterojunction is observed around 40% in the visible region, which rapidly drops to 17% from 0 to 0.86 eV. It again starts to increase toward higher energy ranges, and a maximum reflection of around 30% is observed between energy ranges from 4.5 to 10 eV in the UV region. It is worth mentioning that the electron−hole interaction is not taken into account while calculating the optical properties of SnS, TaS_2, and SnS/TaS_2 heterojunction in this study. The GW approximation combined with the Bethe−Salpeter equation (GW + BSE) can accurately describe the optical response by introducing self-energy corrections and capturing excitonic effects.[54] However, it is computationally too expensive for this system due to its large size. We use the Kubo−Greenwood method to calculate the dielectric tensor, where the imaginary part is the sum of occupied and unoccupied bands of the dipole matrix elements. Our calculated results can provide a qualitative understanding of the optical behavior of this system.

We chose the configuration with the minimum number of atoms. To check the dependency of results on interface configurations, we also carried out additional calculations for another model following the same procedure. The main results are found to be consistent with each other, which confirms the reliability of our heterojunction model. Details can be found in the Supporting Information.

SUMMARY

In this work, we have studied the vdW heterostructure composed of SnS and TaS_2 monolayers by treating them as the channel material and electrode because of their intrinsic semiconducting and metallic features, respectively. The energetic and thermal stabilities are confirmed by the binding energy calculation and AIMD simulations. A detailed analysis of the electronic structures indicates that (1) an ohmic contact is naturally formed because the Fermi level of the heterostructure moves into the valance bands of SnS; (2) a tunneling barrier is also found at the vdW gap, where the weak orbital overlap leads to a relatively small tunneling possibility of 26.67%; (3) holes can freely move from the electrode to the channel region due to the upward band bending; (4) the contact causes enhanced optical responses, especially in the visible and UV ranges, for the SnS/TaS_2 heterojunction as compared with the freestanding monolayers. These findings together with the synthesis of the SnS/TaS_2 superlattice will trigger more experimental studies on the electronic and optoelectronic devices based on the SnS/TaS_2 heterostructure.

ASSOCIATED CONTENT

Supporting Information

The Supporting Information is available free of charge at https://pubs.acs.org/doi/10.1021/acsami.1c16020.

Top view and side view of the optimized structure; projected band structure of TaS_2 and SnS onto SnS/TaS_2 heterojunction; total potential energy fluctuation with the AIMD simulation; band alignment; comparison of the main results between case 1 and case 2; imaginary part of the dielectric function, absorption coefficient, optical conductivity, and reflectivity percentage for SnS and TaS_2 monolayers, and the SnS−TaS_2 heterojunction (PDF)

AUTHOR INFORMATION

Corresponding Authors

Yaguang Guo − *Department of Physics, School of Science, Beijing Jiaotong University, Beijing 100044, China*; Email: ygguo@bjtu.edu.cn

Qian Wang − *School of Materials Science and Engineering, Peking University, Beijing 100871, China; Center for Applied Physics and Technology, HEPDS, College of Engineering, Peking University, Beijing 100871, China*; orcid.org/0000-0002-9766-4617; Email: qianwang2@pku.edu.cn

Authors

Arzoo Hassan − *School of Materials Science and Engineering, Peking University, Beijing 100871, China*

Muhammad Azhar Nazir − *School of Materials Science and Engineering, Peking University, Beijing 100871, China*

Yiheng Shen − *School of Materials Science and Engineering, Peking University, Beijing 100871, China; Center for Applied Physics and Technology, HEPDS, College of Engineering, Peking University, Beijing 100871, China*

Wei Kang − *Center for Applied Physics and Technology, HEPDS, College of Engineering, Peking University, Beijing 100871, China*

Complete contact information is available at: https://pubs.acs.org/10.1021/acsami.1c16020

Notes

The authors declare no competing financial interest.

ACKNOWLEDGMENTS

This work is partially supported by grants from the National Key Research and Development Program of the Ministry of Science and Technology of China (Grant No. 2017YFA0205003) and the National Natural Science Foundation of China (Grant Nos. 12104037, 21773004, and 11974028). Y.G. acknowledges support from the Fundamental Research Funds for the Central Universities (2021JBM041). The study is also supported by the High-Performance Computing Platform of Peking University, China.

REFERENCES

(1) Zhao, L.-D.; Lo, S.-H.; Zhang, Y.; Sun, H.; Tan, G.; Uher, C.; Wolverton, C.; Dravid, V. P.; Kanatzidis, M. G. Ultralow thermal conductivity and high thermoelectric figure of merit in SnSe crystals. *Nature* **2014**, *508*, 373−377.

(2) Zhao, L.-D.; Tan, G.; Hao, S.; He, J.; Pei, Y.; Chi, H.; Wang, H.; Gong, S.; Xu, H.; Dravid, V. P.; et al. Ultrahigh power factor and thermoelectric performance in hole-doped single-crystal SnSe. *Science* **2016**, *351*, 141−144.

(3) Iguchi, Y.; Inoue, K.; Sugiyama, T.; Yanagi, H. Single-crystal growth of Cl-doped n-type SnS using SnCl2 self-flux. *Inorg. Chem.* **2018**, *57*, 6769−6772.
(4) Steinmann, V.; Jaramillo, R.; Hartman, K.; Chakraborty, R.; Brandt, R. E.; Poindexter, J. R.; Lee, Y. S.; Sun, L.; Polizzotti, A.; Park, H. H.; et al. 3.88% efficient tin sulfide solar cells using congruent thermal evaporation. *Adv. Mater.* **2014**, *26*, 7488−7492.
(5) Sinsermsuksakul, P.; Hartman, K.; Bok Kim, S.; Heo, J.; Sun, L.; Hejin Park, H.; Chakraborty, R.; Buonassisi, T.; Gordon, R. G. Enhancing the efficiency of SnS solar cells via band-offset engineering with a zinc oxysulfide buffer layer. *Appl. Phys. Lett.* **2013**, *102*, No. 053901.
(6) Sinsermsuksakul, P.; Sun, L.; Lee, S. W.; Park, H. H.; Kim, S. B.; Yang, C.; Gordon, R. G. Overcoming efficiency limitations of SnS-based solar cells. *Adv. Energy Mater.* **2014**, *4*, No. 1400496.
(7) Kawanishi, S.; Suzuki, I.; Bauers, S. R.; Zakutayev, A.; Shibata, H.; Yanagi, H.; Omata, T. SnS Homojunction Solar Cell with n-Type Single Crystal and p-Type Thin Film. *Sol. RRL* **2021**, *5*, No. 2000708.
(8) Tian, Z.; Guo, C.; Zhao, M.; Li, R.; Xue, J. Two-dimensional SnS: a phosphorene analogue with strong in-plane electronic anisotropy. *ACS Nano* **2017**, *11*, 2219−2226.
(9) Zhang, Y.; Lu, J.; Shen, S.; Xu, H.; Wang, Q. Ultralarge single crystal SnS rectangular nanosheets. *Chem. Commun.* **2011**, *47*, 5226−5228.
(10) Brent, J. R.; Lewis, D. J.; Lorenz, T.; Lewis, E. A.; Savjani, N.; Haigh, S. J.; Seifert, G.; Derby, B.; O'Brien, P. Tin (II) sulfide (SnS) nanosheets by liquid-phase exfoliation of herzenbergite: IV−VI main group two-dimensional atomic crystals. *J. Am. Chem. Soc.* **2015**, *137*, 12689−12696.
(11) Li, S.; Zheng, J.; Zuo, S.; Wu, Z.; Yan, P.; Pan, F. 2D hybrid anode based on SnS nanosheet bonded with graphene to enhance electrochemical performance for lithium-ion batteries. *RSC Adv.* **2015**, *5*, 46941−46946.
(12) Fei, R.; Li, W.; Li, J.; Yang, L. Giant piezoelectricity of monolayer group IV monochalcogenides: SnSe, SnS, GeSe, and GeS. *Appl. Phys. Lett.* **2015**, *107*, No. 173104.
(13) Wu, M.; Zeng, X. C. Intrinsic ferroelasticity and/or multiferroicity in two-dimensional phosphorene and phosphorene analogues. *Nano Lett.* **2016**, *16*, 3236−3241.
(14) Wang, H.; Qian, X. Giant optical second harmonic generation in two-dimensional multiferroics. *Nano Lett.* **2017**, *17*, 5027−5034.
(15) Suzuki, I.; Kawanishi, S.; Bauers, S. R.; Zakutayev, A.; Lin, Z.; Tsukuda, S.; Shibata, H.; Kim, M.; Yanagi, H.; Omata, T. N-Type Electrical Conduction in SnS Thin Films. *Physical Review Materials* **2021**, *5* (12), 125405.
(16) Schulman, D. S.; Arnold, A. J.; Das, S. Contact engineering for 2D materials and devices. *Chem. Soc. Rev.* **2018**, *47*, 3037−3058.
(17) Hajzus, J. R.; Biacchi, A. J.; Le, S. T.; Richter, C. A.; Walker, A. R. H.; Porter, L. M. Contacts to solution-synthesized SnS nanoribbons: dependence of barrier height on metal work function. *Nanoscale* **2018**, *10*, 319−327.
(18) Li, S.; Xiao, W.; Pan, Y.; Jie, J.; Xin, C.; Zheng, J.; Lu, J.; Pan, F. Interfacial properties of monolayer SnS−metal contacts. *J. Phys. Chem. C* **2018**, *122*, 12322−12331.
(19) Padilha, J.; Fazzio, A.; da Silva, A. J. van der Waals heterostructure of phosphorene and graphene: tuning the Schottky barrier and doping by electrostatic gating. *Phys. Rev. Lett.* **2015**, *114*, No. 066803.
(20) Yankowitz, M.; Ma, Q.; Jarillo-Herrero, P.; LeRoy, B. J. van der Waals heterostructures combining graphene and hexagonal boron nitride. *Nat. Rev. Phys.* **2019**, *1*, 112−125.
(21) Zollner, K.; Gmitra, M.; Fabian, J. Heterostructures of graphene and hBN: Electronic, spin-orbit, and spin relaxation properties from first principles. *Phys. Rev. B* **2019**, *99*, No. 125151.
(22) Ebnonnasir, A.; Narayanan, B.; Kodambaka, S.; Ciobanu, C. V. Tunable MoS2 bandgap in MoS2-graphene heterostructures. *Appl. Phys. Lett.* **2014**, *105*, No. 031603.
(23) Zhao, C.; Wang, X.; Kong, J.; Ang, J. M.; Lee, P. S.; Liu, Z.; Lu, X. Self-assembly-induced alternately stacked single-layer MoS2 and N-doped graphene: A novel van der Waals heterostructure for lithium-ion batteries. *ACS Appl. Mater. Interfaces* **2016**, *8*, 2372−2379.
(24) Pierucci, D.; Henck, H.; Avila, J.; Balan, A.; Naylor, C. H.; Patriarche, G.; Dappe, Y. J.; Silly, M. G.; Sirotti, F.; Johnson, A. C.; et al. Band alignment and minigaps in monolayer MoS2-graphene van der Waals heterostructures. *Nano Lett.* **2016**, *16*, 4054−4061.
(25) Geng, H.; Yuan, D.; Yang, Z.; Tang, Z.; Zhang, X.; Yang, K.; Su, Y. Graphene van der Waals heterostructures for high-performance photodetectors. *J. Mater. Chem. C* **2019**, *7*, 11056−11067.
(26) Kang, J.; Jariwala, D.; Ryder, C. R.; Wells, S. A.; Choi, Y.; Hwang, E.; Cho, J. H.; Marks, T. J.; Hersam, M. C. Probing out-of-plane charge transport in black phosphorus with graphene-contacted vertical field-effect transistors. *Nano Lett.* **2016**, *16*, 2580−2585.
(27) Xiong, W.; Xia, C.; Zhao, X.; Wang, T.; Jia, Y. Effects of strain and electric field on electronic structures and Schottky barrier in graphene and SnS hybrid heterostructures. *Carbon* **2016**, *109*, 737−746.
(28) Roberts, D. M.; Bardgett, D.; Gorman, B. P.; Perkins, J. D.; Zakutayev, A.; Bauers, S. R. Synthesis of tunable SnS-TaS2 nanoscale superlattices. *Nano Lett.* **2020**, *20*, 7059−7067.
(29) Navarro-Moratalla, E.; Island, J. O.; Manas-Valero, S.; Pinilla-Cienfuegos, E.; Castellanos-Gomez, A.; Quereda, J.; Rubio-Bollinger, G.; Chirolli, L.; Silva-Guillén, J. A.; Agraït, N.; et al. Enhanced superconductivity in atomically thin TaS 2. *Nat. Commun.* **2016**, *7*, No. 11043.
(30) Yang, Y.; Navarro-Moratalla, E.; Watanabe, K.; Taniguchi, T.; Jarillo-Herrero, P. In *Enhanced Superconductivity in Atomically Thin 2H-TaS_2 Down to the Ultra-Thin Limit*, APS March Meeting Abstracts, 2017; p 39.007.
(31) Sharma, S.; Auluck, S.; Khan, M. Optical properties of 1T and 2H phase of TaS 2 and TaSe 2. *Pramana* **2000**, *54*, 431−440.
(32) Kresse, G.; Furthmüller, J. Efficient iterative schemes for ab initio total-energy calculations using a plane-wave basis set. *Phys. Rev. B* **1996**, *54*, No. 11169.
(33) Kresse, G.; Joubert, D. From ultrasoft pseudopotentials to the projector augmented-wave method. *Phys. Rev. B* **1999**, *59*, No. 1758.
(34) Blöchl, P. E. Projector augmented-wave method. *Phys. Rev. B* **1994**, *50*, No. 17953.
(35) Perdew, J. P.; Burke, K.; Ernzerhof, M. Generalized gradient approximation made simple. *Phys. Rev. Lett.* **1996**, *77*, No. 3865.
(36) Klimeš, J.; Bowler, D. R.; Michaelides, A. Chemical accuracy for the van der Waals density functional. *J. Phys.: Condens. Matter* **2009**, *22*, No. 022201.
(37) Klimeš, J.; Bowler, D. R.; Michaelides, A. Van der Waals density functionals applied to solids. *Phys. Rev. B* **2011**, *83*, No. 195131.
(38) Monkhorst, H. J.; Pack, J. D. Special points for Brillouin-zone integrations. *Phys. Rev. B* **1976**, *13*, No. 5188.
(39) Hassan, A.; Guo, Y.; Wang, Q. Performance of the pentagonal PdSe2 sheet as a channel material in contact with metal surfaces and graphene. *ACS Appl. Electron. Mater.* **2020**, *2*, 2535−2542.
(40) Nosé, S. A unified formulation of the constant temperature molecular dynamics methods. *J. Chem. Phys.* **1984**, *81*, 511−519.
(41) Liu, Q.-J.; Liu, Z.-T.; Feng, L.-P. Elasticity, electronic structure, chemical bonding and optical properties of monoclinic ZrO2 from first-principles. *Phys. B: Condens. Matter* **2011**, *406*, 345−350.
(42) Gomes, L. C.; Carvalho, A. Phosphorene analogues: Isoelectronic two-dimensional group-IV monochalcogenides with orthorhombic structure. *Phys. Rev. B* **2015**, *92*, No. 085406.
(43) Conroy, L. E.; Pisharody, K. R. The preparation and properties of single crystals of the 1S and 2S polymorphs of tantalum disulfide. *J. Solid State Chem.* **1972**, *4*, 345−350.
(44) Guo, Y.; Wang, F. Q.; Wang, Q. An all-carbon vdW heterojunction composed of penta-graphene and graphene: tuning the Schottky barrier by electrostatic gating or nitrogen doping. *Appl. Phys. Lett.* **2017**, *111*, No. 073503.
(45) Zhou, W.; Guo, Y.; Liu, J.; Wang, F. Q.; Li, X.; Wang, Q. 2D SnSe-based vdW heterojunctions: tuning the Schottky barrier by reducing Fermi level pinning. *Nanoscale* **2018**, *10*, 13767−13772.

https://doi.org/10.1021/acsami.1c16020
ACS Appl. Mater. Interfaces 2022, 14, 2177−2184

(46) Mao, Y.; Xu, C.; Yuan, J.; Zhao, H. A two-dimensional GeSe/SnSe heterostructure for high performance thin-film solar cells. *J. Mater. Chem. A* **2019**, *7*, 11265−11271.
(47) Peng, Q.; Wang, Z.; Sa, B.; Wu, B.; Sun, Z. Electronic structures and enhanced optical properties of blue phosphorene/transition metal dichalcogenides van der Waals heterostructures. *Sci. Rep.* **2016**, *6*, No. 31994.
(48) Rudin, S. P.; Johnson, D. C. Density functional theory calculations of the turbostratically disordered compound [(SnSe) 1+ y] m (VSe 2) n. *Phys. Rev. B* **2015**, *91*, No. 144203.
(49) Geim, A. K.; Grigorieva, I. V. Van der Waals heterostructures. *Nature* **2013**, *499*, 419−425.
(50) Novoselov, K.; Mishchenko, A.; Carvalho, A.; Neto, A. C. 2D materials and van der Waals heterostructures. *Science* **2016**, *353*, No. eaac9439.
(51) Xu, L.; Zhang, P.; Jiang, H.; Wang, X.; Chen, F.; Hu, Z.; Gong, Y.; Shang, L.; Zhang, J.; Jiang, K.; et al. Large-scale growth and field-effect transistors electrical engineering of atomic-layer SnS2. *Small* **2019**, *15*, No. 1904116.
(52) Zhong, H.; Quhe, R.; Wang, Y.; Ni, Z.; Ye, M.; Song, Z.; Pan, Y.; Yang, J.; Yang, L.; Lei, M. Interfacial properties of monolayer and bilayer MoS 2 contacts with metals: beyond the energy band calculations. *Sci. Rep.* **2016**, *6*, No. 1.
(53) Guo, Y.; Saidi, W. A.; Wang, Q. 2D halide perovskite-based van der Waals heterostructures: contact evaluation and performance modulation. *2D Mater.* **2017**, *4*, No. 035009.
(54) Bruno, M.; Palummo, M.; Marini, A.; Del Sole, R.; Ossicini, S. From Si nanowires to porous silicon: the role of excitonic effects. *Phys. Rev. Lett.* **2007**, *98*, No. 036807.

https://doi.org/10.1021/acsami.1c16020
ACS Appl. Mater. Interfaces 2022, 14, 2177−2184